Supporting information for

Tailoring the Nano Heterointerface of Hematite/Magnetite on Hierarchical Nitrogen-Doped Carbon Nanocages for Superb Oxygen Reduction

Hao Fan,[†] Kun Mao,[†] Meng Liu,[†] Ou Zhuo,[†] Jin Zhao,[†] Tao Sun,[†] Yufei Jiang,[†] Xiao Du,[†] Xiali Zhang,[‡] Qingsong Wu,[‡] Renchao Che,[*,‡] Lijun Yang,[†] Qiang Wu,[†] Xizhang Wang,[*,†] and Zheng Hu[*,†]

[†]Key Laboratory of Mesoscopic Chemistry of MOE and Collaborative Innovation Center of Chemistry for Life Sciences, School of Chemistry and Chemical Engineering, Nanjing University, Nanjing 210023, China
[‡]Laboratory of Advanced Materials, Department of Materials Science and Collaborative Innovation Center of Chemistry for Energy Materials (iChem), Fudan University, Shanghai 200438, China
*E-mail: wangxzh@nju.edu.cn; rcche@fudan.edu.cn; zhenghu@nju.edu.cn.

Electrochemical Calculations

In order to explore the oxygen reduction reaction (ORR) in a more quantitative manner, the number of electrons transferred per O_2 molecule (n) in the ORR process is determined using Koutecky-Levich equation (S1) and (S2) according to the LSV data.

$$\frac{1}{j} = \frac{1}{B\omega^{\frac{1}{2}}} + \frac{1}{j_K} \tag{S1}$$

$$B = 0.2nFD_{O_2}^{\frac{2}{3}} v^{-\frac{1}{6}} C_{O_2} \tag{S2}$$

where, j_K is the kinetic current density, ω is the electrode rotating rate (rpm), F is the Faraday constant (96485 C mol^{-1}), C_{O2} is the bulk concentration of O_2 (1.2×10^{-3} mol L^{-1}), v is the kinematic viscosity of the electrolyte (0.01 cm^2 s^{-1}), and D_{O2} is the diffusion coefficient of O_2 in 0.1 mol L^{-1} KOH (1.9×10^{-5} cm^2 s^{-1}).[1]

In addition, n and the corresponding productivity of peroxide species ($\%HO_2^-$) were also calculated by the following equation (S3) and (S4) according to the rotating ring-disk electrode (RRDE) data.

$$n = 4 \times \frac{I_d}{I_d + I_r/N} \tag{S3}$$

$$\%HO_2^- = 200 \times \frac{I_r/N}{I_d + I_r/N} \tag{S4}$$

where, I_d and I_r were the disk electrode current and ring electrode current, respectively. Pt ring electrode is polarized at 0.5 V (vs. Ag/AgCl), and N is the collection efficiency at the ring electrode (N=0.35).
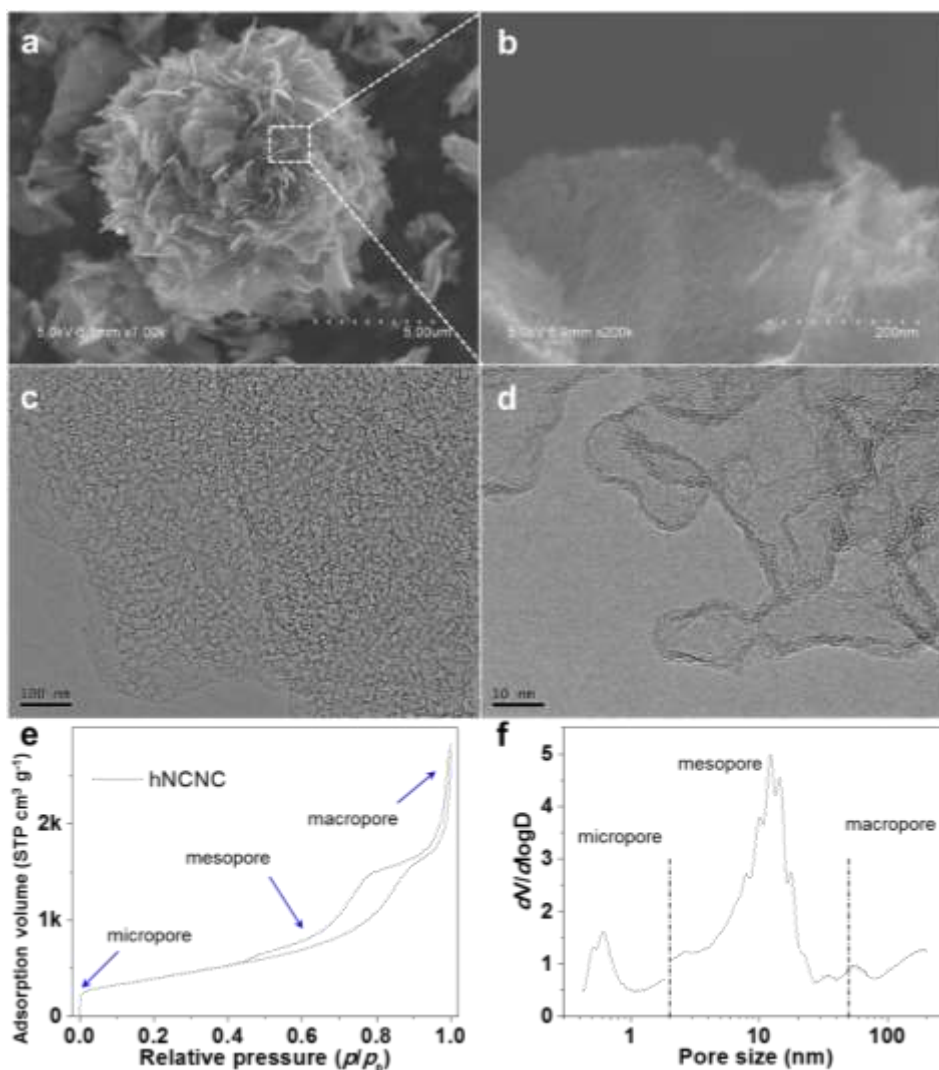
Fig. S1. Morphology and structure characterizations of hNCNC support. (a,b) low- and high-magnification SEM images. (c,d) low- and high-magnification TEM images. (e) N_2 adsorption/desorption isotherms. (f) The corresponding pore size distribution calculated from the adsorption branch of the isotherm using Horvath-Kawazoe (HK, for micropores) and Barrett-Joyner-Halenda (BJH, for mesopores) methods, respectively. The specific surface area was calculated using the Brunauer-Emmett-Teller (BET) method based on the adsorption data in the linear relative pressure (p/p_0) range of 0.05-0.30.

The hNCNC support has a unique hierarchical structure with network geometry and micro-sized carbon nanosheets (Fig. S1a,b). The nanosheets are composed of the interconnected nanocages with ca. 20-50 nm in size and ca. 3-7 well-graphitized layers in thickness (Fig. S1c,d). The unique geometry endows hNCNC with a large specific surface area of 1430 m^2 g^{-1}, coexisting micro-meso-macropores (Fig. S1e,f), and a good conductivity of 290 S m^{-1} (Table S1). The hCNC support has the similar characteristics with hNCNC (Table S1).[2]
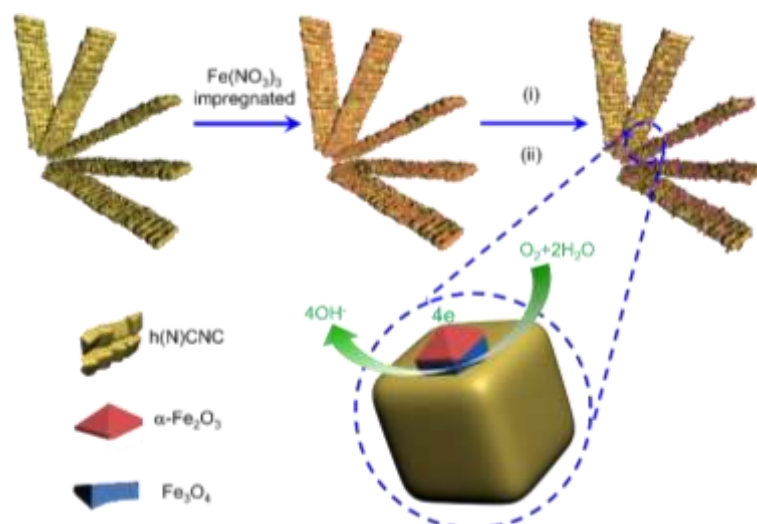
Scheme S1. Schematic diagram of construction and oxygen reduction mechanism for heterostructural α-Fe$_2$O$_3$/Fe$_3$O$_4$/h(N)CNC catalysts. The interfaced Fe$_3$O$_4$ species between the nanocrystals and h(N)CNC supports are controllably adjusted by two strategies: (i) heating at the temperatures of 350, 400, 450, 500, and 550 °C for 2.0 h and (ii) heating at 400 °C with the time for 0.5, 1, 1.5, 4, and 6 h, respectively.
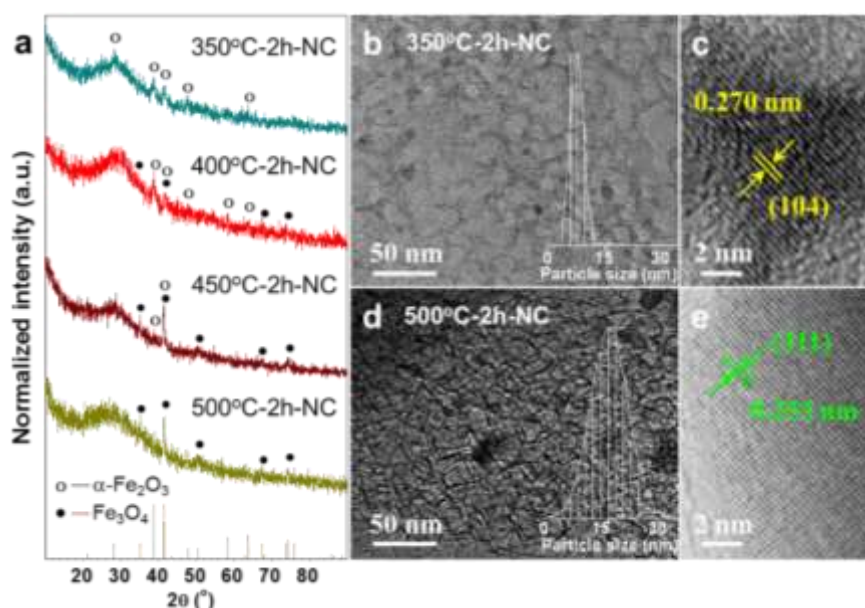
Fig. S2. XRD and TEM characterizations. (a) XRD patterns of the α-Fe$_2$O$_3$/Fe$_3$O$_4$/hNCNC catalysts treated at 350, 400, 450, and 500 °C, respectively. o: α-Fe$_2$O$_3$ (JCPDS No. 33-0664); •: Fe$_3$O$_4$ (JCPDS No. 85-1438). (b-e) Low- and high-magnification TEM images of the 350°C-2h-NC (b,c) and 500°C-2h-NC (d,e), respectively. The insets in (b) and (d) are the particle size distributions from 500 nanoparticles. The fringe separations of 0.270 and 0.296 nm correspond to the d_{104} of α-Fe$_2$O$_3$ and d_{220} of Fe$_3$O$_4$.

The iron oxide in 350°C-2h-NC and 400°C-2h-NC mainly exists as α-Fe$_2$O$_3$ phase while, in 450°C-2h-NC and 500°C-2h-NC, it primarily transforms into Fe$_3$O$_4$ phase based on the changes involving a great intensity reduction of the peak for α-Fe$_2$O$_3$ at 38.6°, four disappeared peaks of α-Fe$_2$O$_3$ at 28.1, 47.8, 58.2, and 63.7°, three new formed peaks of Fe$_3$O$_4$ at 35.1, 50.5 and 67.3°, and the significant intensity increment of the peak of Fe$_3$O$_4$ at 41.4° (Fig. S2a). TEM characterizations show that the iron oxide nanocrystals are highly dispersed on hNCNC with the average sizes of 8.4 nm for 350°C-2h-NC, 8.9 nm for 400°C-2h-NC, 13.6 nm for 400°C-6h-NC, and 17.2 nm for 500°C-2h-NC, and with the close loadings of ca. 16.9, 16.6, 16.8, and 16.5 wt.%, respectively (Fig. 1b,d in main text, Fig. S2b,c and Fig. S3). The larger particle sizes for the latter two catalysts than the former two could be ascribed to the particle migration and aggregation with increasing heating time and

temperature. The fringe separations of 0.270 and 0.253 nm in HRTEM images are corresponding to d_{104} of α-Fe_2O_3 and the d_{311} of Fe_3O_4 (Fig. 1c,e in main text and Fig. S2d,e). The evolution from α-Fe_2O_3 to Fe_3O_4 is consistent with the XRD measurements (Fig. S2a).
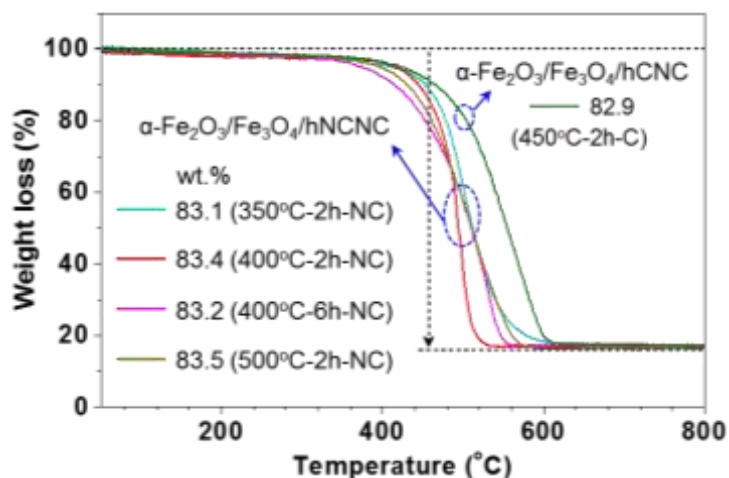
Fig. S3. TGA curves of the typical catalysts. The weight losses for the catalysts are 83.1, 83.4, 83.2, 83.5, and 82.9 wt.%, respectively, i.e., corresponding to the close loadings of 16.9, 16.6, 16.8, 16.5 and 17.1 wt.%.
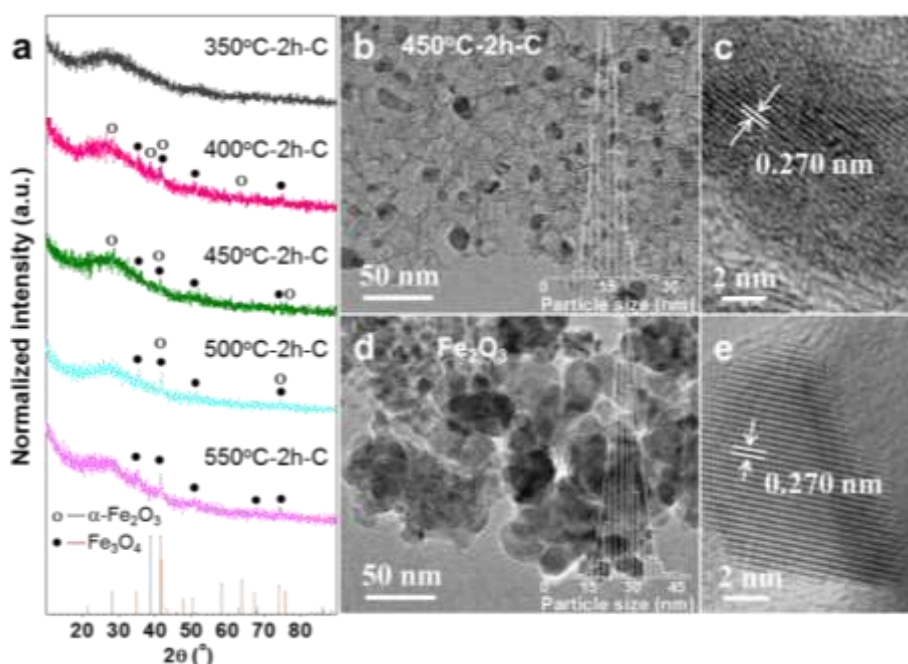
Fig. S4. XRD and TEM characterizations. (a) XRD patterns of the α-Fe_2O_3/Fe_3O_4/hCNC catalysts treated at 350, 400, 450, 500, and 550 °C, respectively. o: α-Fe_2O_3 (JCPDS No. 33-0664); •: Fe_3O_4 (JCPDS No. 85-1438). (b-e) Low- and high-magnification TEM images of the 450°C-2h-C (b,c) and pure α-Fe_2O_3 (d,e), respectively. The insets in (b) and (d) are the particle size distributions from 500 nanoparticles. The fringe separation of 0.270 nm corresponds to the d_{104} of α-Fe_2O_3.

For 350°C-2h-C, no diffraction peaks of α-Fe_2O_3 and Fe_3O_4 are observed, ascribed to the poor crystallinity. With the temperature increasing to 400 and 450 °C, the diffraction peaks at 28.1, 38.6, 41.6, and 74.0° are corresponded to α-Fe_2O_3 phase along with the increased intensity. After 450 °C, the catalysts have the emerging peaks at 35.1 and 50.5°, which are assigned to the Fe_3O_4 phase. For 550°C-2h-C, the iron oxides are Fe_3O_4-dominated based on the analyses of one new formed peak at 67.3°, two disappeared peaks of α-Fe_2O_3 at 28.1 and 38.6°, and the significant increment of the peak intensity at 41.4° (Fig. S4a). Thus, the hetero-α-Fe_2O_3/Fe_3O_4 nanocrystals loaded on undoped hCNC support is controllable synthesis by adjusting heating temperatures. The typical 450°C-2h-C with

the average size of 14.5 nm shows the fringe separation of 0.270 nm, which corresponds to the d_{104} of α-Fe_2O_3 (Fig. S4b,c). The pure α-Fe_2O_3 has the even larger particles with the average size of 27.2 nm (Fig. S4d,e). These results are in accordance with the XRD results (Fig. S4a).
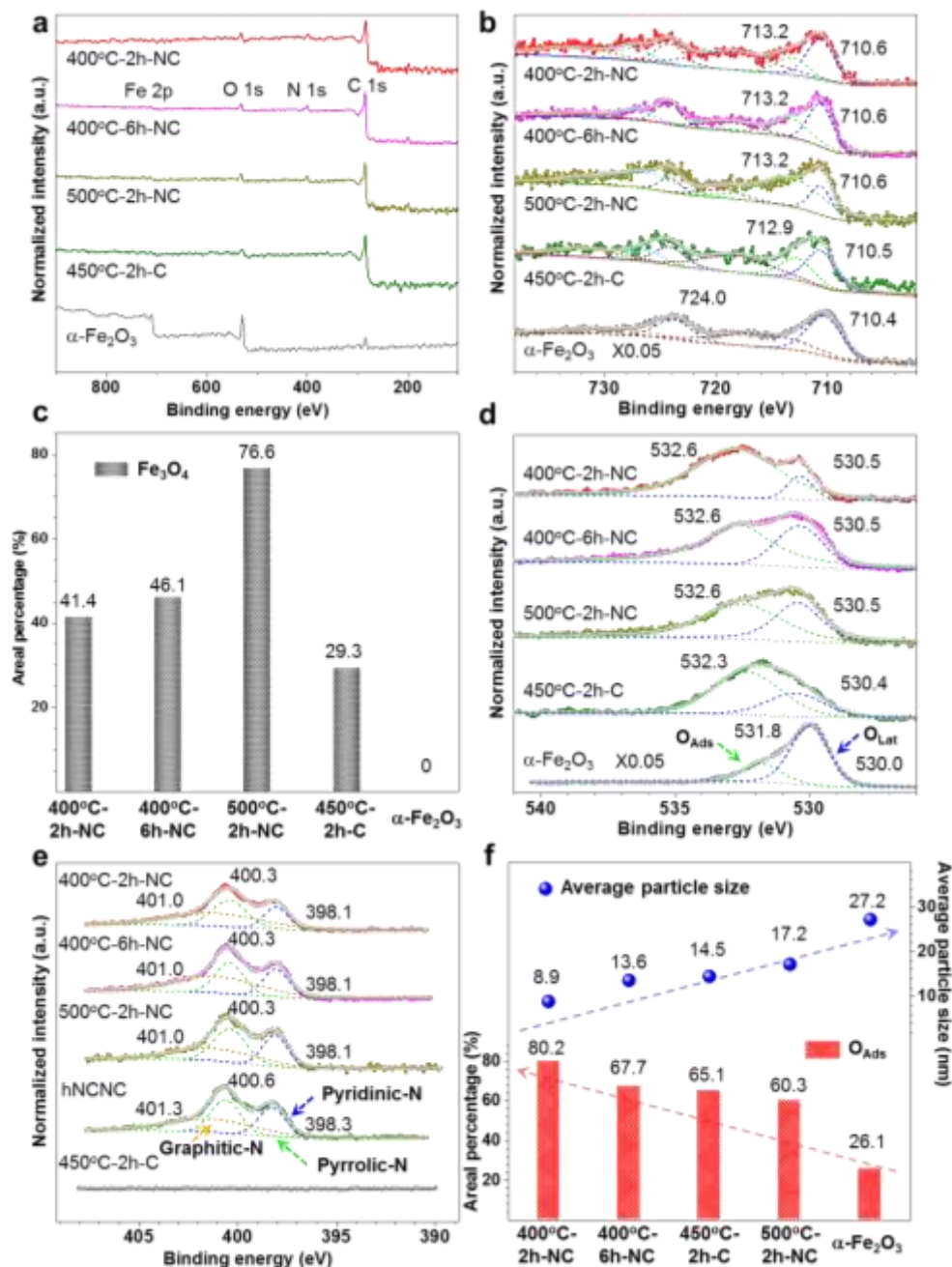
Fig. S5. XPS analyses on the catalysts. (a) Full survey spectra. (b) Fe 2p. (c) The areal percentage of Fe_3O_4 species. (d) O 1s. (e) N 1s. (f) The areal percentage change of O_{Ads} species versus the respective average particle size. XPS spectrum of pure α-Fe_2O_3 is also presented for comparison with the intensity multiplied by 0.05.

For the control sample of pure α-Fe_2O_3, the Fe 2p peaks at 710.4 eV (Fe $2p_{3/2}$) and 724.0 eV (Fe $2p_{1/2}$) with respective satellite peaks at ca. 718 and 732 eV are the characteristic of Fe^{3+}.[3-5] The O 1s peaks at 530.0 and 531.8 eV are assigned to the lattice oxygen (O_{Lat}) and adsorbed oxygen (O_{Ads}) species with the former as the predominant (Fig. S5b-d).[4, 6-10] For the series of α-Fe_2O_3/Fe_3O_4/hNCNC catalysts, a new Fe 2p peak at 713.2 eV indicates the existence of Fe_3O_4 species.[3, 4] The areal percentage of Fe_3O_4 species increases from 41.4% of 400°C-2h-NC to 46.1% of 400°C-6h-NC, and 76.6% of 500°C-2h-NC, as expected due to the increase of carbothermal reduction, which are higher than 29.3% of 450°C-2h-C (Fig. S5c). The O 1s peaks at 530.5 (O_{Lat})

and 532.6 eV (O_{Ads}) show the big positive shifts of 0.5 and 0.8 eV with the latter as the predominant (Fig. S5b,d). The similar cases but with less degree for α-Fe_2O_3/Fe_3O_4/hCNC (450°C-2h-C) were also observed (Fig. S5b,d). In contrast, the N 1s peaks of α-Fe_2O_3/Fe_3O_4/hNCNC, which mainly come from three N species of pyridinic-N (ca. 398.1 eV), pyrrolic-N (ca. 400.3 eV), and graphitic-N (ca. 401.0 eV), respectively, have the slight negative shifts of ca. 0.2-0.3 eV in comparison with the cases of hNCNC support (Fig. 5e). The opposite shifts, i.e., the positive shifts of Fe 2p, O 1s and negative shift of N 1s, indicate the charge transfers from α-Fe_2O_3/Fe_3O_4 to hNCNC, reflecting the strong interaction between them. The areal percentage of O_{Ads} species increases from 26.1% of pure α-Fe_2O_3 to 60.3% of 500°C-2h-NC, and to 65.1% of 450°C-2h-C, and to 67.7% of 400°C-6h-NC and 80.2% of 400°C-2h-NC, which mainly results from the gradually reduced average sizes of nanocrystals on h(N)CNC supports (Fig. S5f).

The results of O 1s are in consistent with our early investigations,[9] can be used as an indicator to understand the changes of size, chemical environment and modified electronic states for the nanocrystals.[9, 11] The XPS analyses are well in agreement with the XRD, HRTEM, and EELS characterization results (Fig. 1 and Fig. 2 in main text), which suggest the controllable tailoring of nano heterointerface of α-Fe_2O_3/Fe_3O_4 nanocrystals on h(N)CNC supports.
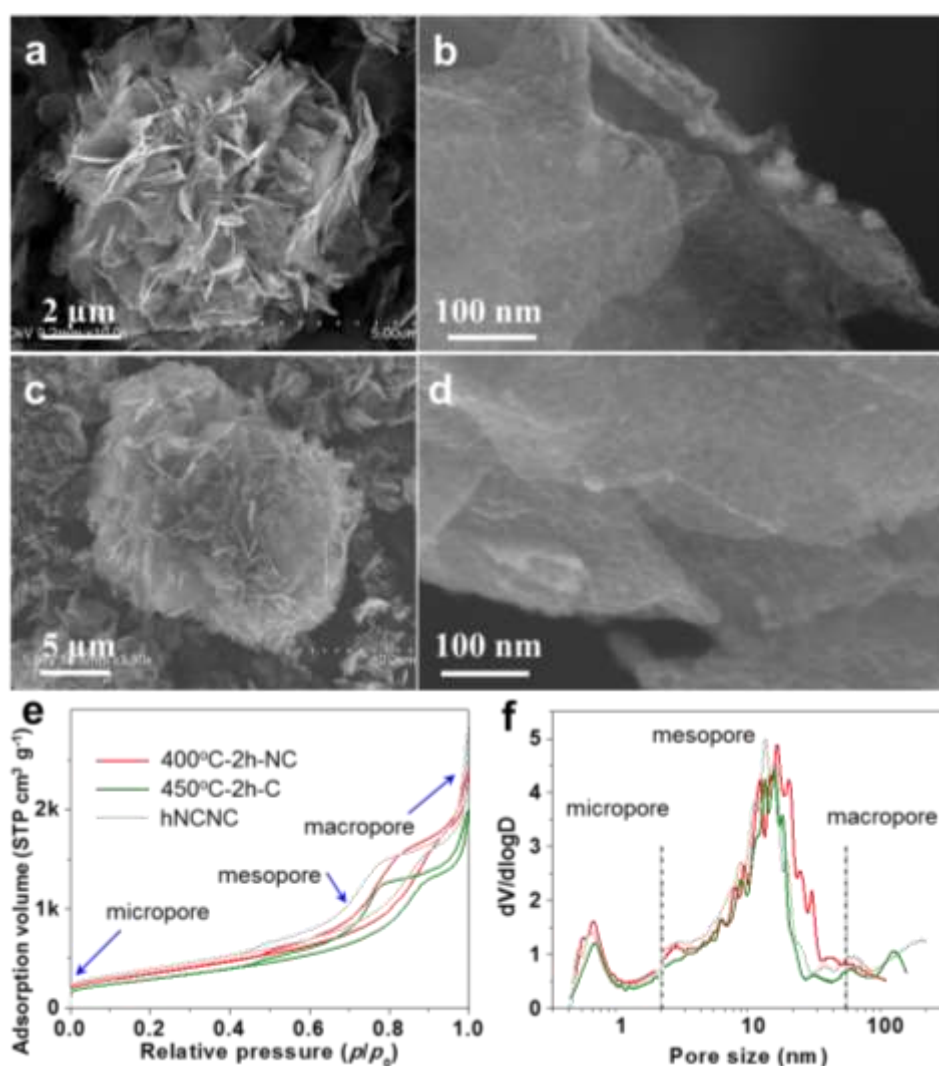
Fig. S6. Morphology and structure characterizations of the typical catalysts. (a-d) Low- and high-magnification SEM images of 400°C-2h-NC (a,b) and 450°C-2h-C (c,d), respectively. (e,f) N_2 adsorption/desorption isotherms (e) and the corresponding pore size distributions (f). The corresponding curves for hNCNC are plotted for comparison.

SEM images for two typical α-Fe_2O_3/Fe_3O_4/hNCNC (400°C-2h-NC) and α-Fe_2O_3/Fe_3O_4/hCNC (450°C-2h-C) reveal the well-maintained hierarchical structure with the supports (Fig. S1a,b, S6a,c).

The nanocrystals are closely decorated on the micro-sized nanosheets (Fig. S6b,d). The N_2 adsorption/desorption measurements for the two catalysts show the typical IV-type isotherms with the approximate specific surface areas of 1250 and 1180 m^2 g^{-1}, respectively, a little smaller than those of each supports (Fig. S6e and Table S1). The corresponding pore size distributions indicate the coexistence of micro-meso-macropores (Fig. S6f). The bulk conductivities (κ) for 400°C-2h-NC (165 S m^{-1}) and 450°C-2h-C (202 S m^{-1}) are five orders of magnitude larger than that of pure α-Fe_2O_3 of 6.10×10^{-4} S m^{-1} (Table S1). The unique hierarchical structure, multi-scale porous and good conductivity favor the charge (ions and electrons) transfer, mass transport, and active sites exposure during electrochemical reactions.
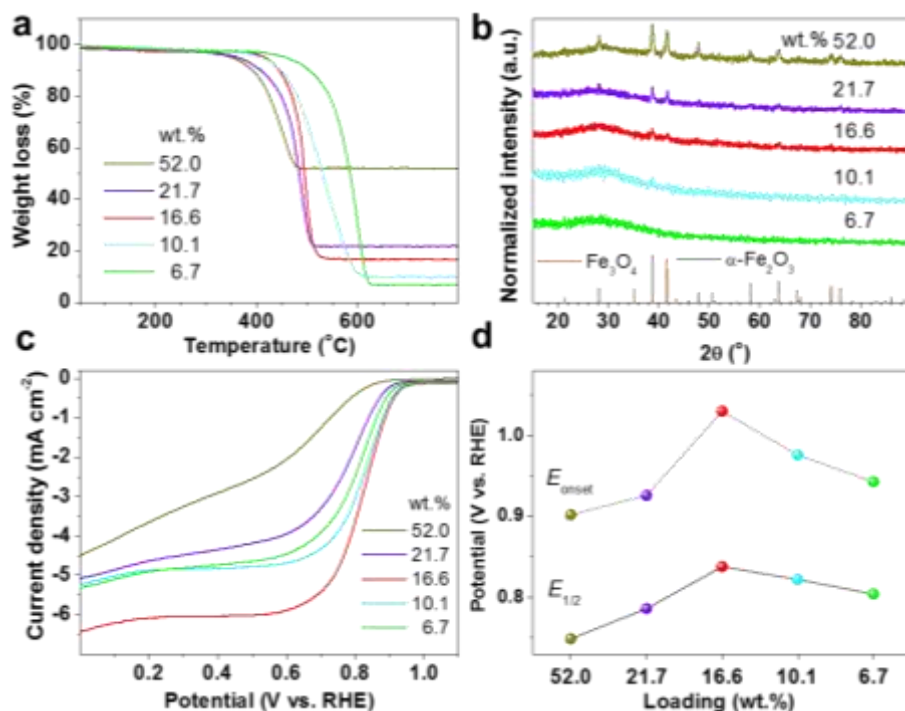
Fig. S7. Structure, composition and ORR performances of α-Fe_2O_3/Fe_3O_4/hNCNC catalysts with various α-Fe_2O_3/Fe_3O_4 loadings. (a) TGA curves. (b) XRD patterns. (c) LSV curves. (d) The corresponding E_{onset} and $E_{1/2}$ diagrams.

With increasing α-Fe_2O_3/Fe_3O_4 content, the ORR activities of α-Fe_2O_3/Fe_3O_4/hNCNC catalysts first increase and then decrease (Fig. S7). And the catalyst with 16.6 wt.% loading delivers the highest ORR performance, including the highest E_{onset} (1.030 V) and $E_{1/2}$ (0.838 V).
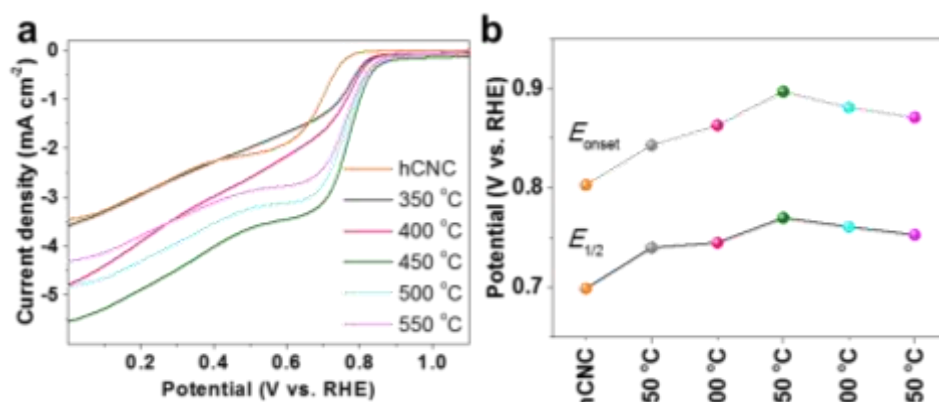
Fig. S8. ORR activities of the α-Fe_2O_3/Fe_3O_4/hCNC catalysts. (a) LSV curves. (b) The corresponding E_{onset} and $E_{1/2}$ diagrams. The ORR activity of hCNC is presented for comparison.

Table S1 Specific surface area, bulk conductivity and composition of the catalysts.

Catalysts	S_{BET} (m^2 g^{-1})	κ (S m^{-1})	Atomic concentrations (at.%)			
			C	N	O	Fe
400°C-2h-NC	1250	165	86.3	7.0	5.7	1.0
450°C-2h-C	1180	202	90.7	-	8.1	1.2
Pure α-Fe$_2$O$_3$	-	6.10×10^{-4}	-	-	68.1	31.9
hNCNC	1430	300	90.9	7.5	1.6	-
hCNC	1390	450	98.6	-	1.4	-

Note: S_{BET} is BET specific surface area. κ is bulk conductivity, measured by a four-wire method using Keithley 6430 source-measure unit (SMU) under 30 MPa pressure.[2]

Table S2 ORR activities of the catalysts in this study.

Catalysts	Conditions		ORR activities		
			E_{onset} (V. vs RHE)	$E_{1/2}$ (V. vs RHE)	J_{L} (mA cm^{-2})
350°C-2h-NC	350 °C		0.914	0.787	3.58
400°C-2h-NC	400 °C	2 h	1.030	0.838	6.02
450°C-2h-NC	450 °C		0.959	0.813	4.84
500°C-2h-NC	500 °C		0.946	0.803	4.48
400°C-0.5h-NC		0.5 h	0.921	0.790	3.98
400°C-1h-NC		1 h	0.945	0.807	4.34
400°C-1.5h-NC	400 °C	1.5 h	0.978	0.821	5.29
400°C-4h-NC		4 h	0.971	0.813	4.96
400°C-6h-NC		6 h	0.962	0.809	4.72
350°C-2h-C	350 °C		0.843	0.740	1.98
400°C-2h-C	400 °C		0.863	0.745	2.60
450°C-2h-C	450 °C	2 h	0.897	0.770	3.63
500°C-2h-C	500 °C		0.881	0.761	3.22
550°C-2h-C	550 °C		0.871	0.753	2.87
Pt/C	Commercial		0.993	0.831	5.68
hNCNC	800 °C		0.880	0.769	4.14
hCNC	800 °C		0.803	0.699	2.12
Pure α-Fe$_2$O$_3$	400 °C		0.680	0.570	0.38
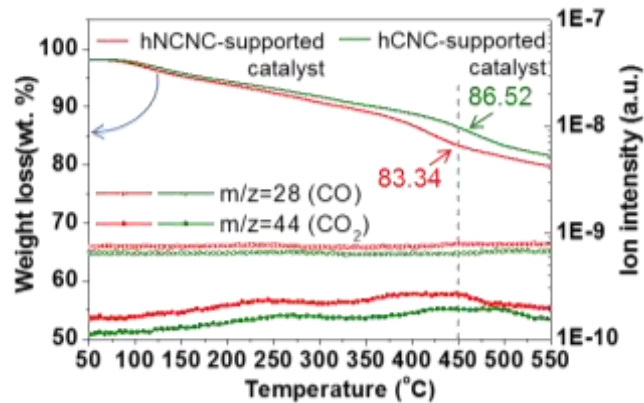
Fig. S9. TGA-MS curves of the typical catalysts with hNCNC and hCNC as support.

For hNCNC-supported catalyst, the mass loss rate is 4.17 wt.% °C^{-1}, which is higher than 3.37 wt.% °C^{-1} for hCNC-supported one. The faster mass loss rate and lower loss-weight temperature for the former than the latter unquestionably indicate that N-doping into carbon could decrease the carbothermal reduction temperature, which could be attributed to the modification of electronic states and the lower wok function via donating a lone pair of electrons of nitrogen.[12-15]
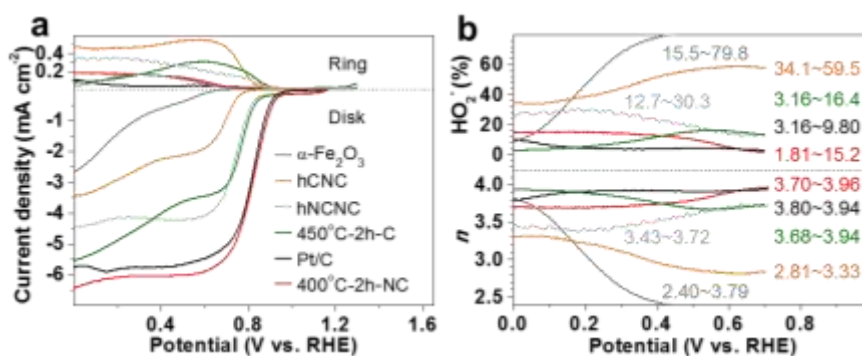
Fig. S10. ORR performances of 400ºC-2h-NC, 450ºC-2h-C, pristine α-Fe₂O₃, hNCNC, hCNC, and Pt/C catalysts. (a) RRDE curves. (b) Plots of *n* and H₂O₂ yield versus potential.
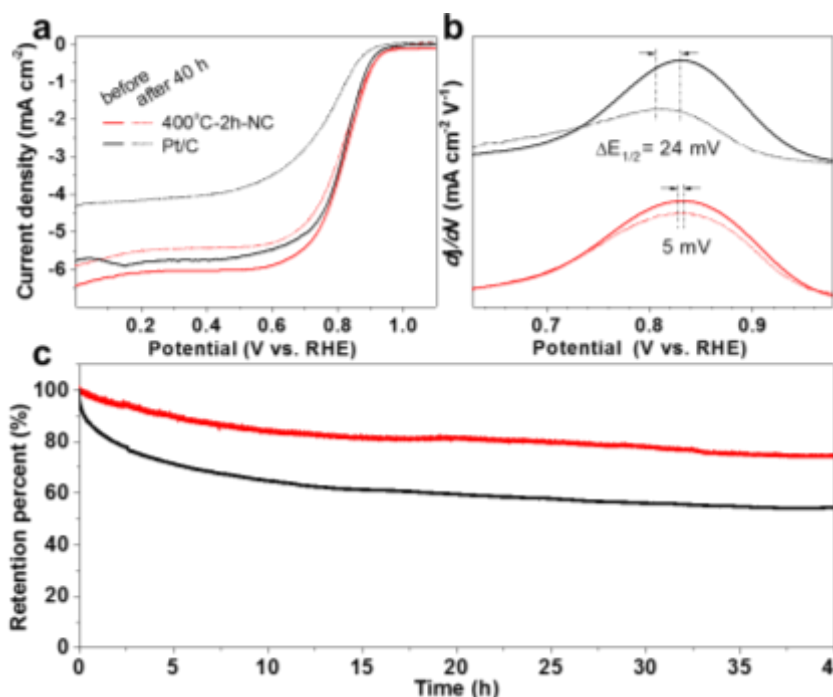
Fig. S11. The durability tests of 400ºC-2h-NC and commercial Pt/C. (a,b) LSV curves before and after 40 h chronoamperometric test (a) and the corresponding differential curves for estimating the shifts of half-wave potential $E_{1/2}$ (b). (c) *I-t* responses at a bias voltage of 0.60 V during 40 h.

Table S3 ORR activity of the optimized α-Fe_2O_3/Fe_3O_4/hNCNC versus the reported transition-metal-based catalysts (Electrolyte: 0.1 mol L^{-1} KOH solution).

Catalysts	S_{BET} (m² g⁻¹)	Particle size (nm)	Catalyst loading (mg cm⁻²)	E_{onset} (V vs. RE)	(V vs. RHE)f	n	Ref.
400°C-2h-NC	1295	8.86	0.12	0.053 (Ag/AgCl)[b]	1.030	3.70-3.96	**This study**
Fe_2O_3/Ppy/GO-800	158	100	0.10	-0.10 (SCE)	0.912	3.58-3.91	16
Fe-Fe_2O_3/NGr	N. A.[a]	3	3.0	0.075 (Hg/HgO)	0.942	3.60	17
α-Fe_2O_3/CNTs	N. A.	~20	0.20	-0.150 (Ag/AgCl)[d]	0.816	3.41-3.83	18
GF+N_2+Fe1_800	450.1	2.6±0.5	0.10	0.907 (RHE)[f]	0.907	4.05	5
Cu-doped Fe_2O_3-PANI-rGO	N. A.	14±2	0.38	-0.0464 (Ag/AgCl)[b]	0.932	3.3-3.9	19
Fe_3O_4/N-C-900	210.6	30-150	0.15	-0.055 (Ag/AgCl)[c]	0.918	3.92	20
Fe_3O_4/N-GAs	N. A.	20-80	0.14	-0.095 (Ag/AgCl)[b]	0.882[e]	3.72-3.95	21
Fe_3O_4/CN_x-Lys	364.7	20	0.20	0.032 (Ag/AgCl)[b]	1.010	3.40-3.60	22
Fe_3O_4/N-GAs	N. A.	50-100	N. A.	-0.090 (Ag/AgCl)[d]	0.876[e]	3.95	23
Fe_3O_4/CN_x/rGO	227	5-10	0.10	-0.145 (Ag/AgCl)[d]	0.822	3.98	24
$FeO_{1.4}$/N-C	N. A.	1	0.25	-0.056 (Ag/AgCl)[d]	0.911	3.10-3.30	25
$MnCoFeO_4$/N-rGO	N. A.	~5	0.10	-0.068 (Ag/AgCl)[b]	0.910	3.80	26
MnO-m-N-C	236	~20	0.10	0.935 (RHE)[e]	0.935	3.80	27
Mn_3O_4/N-graphene	164	5-20	0.10	-0.130 (Ag/AgCl)[b]	0.847	3.81	28
Mn_3O_4/N-graphene	~190	~20	0.25	-0.090 (Ag/AgCl)[b]	0.887	3.85	29
Mn_3O_4@CN_x	N. A.	~100	0.66	0.080 (Hg/HgO)[e]	0.946	~3.60	30
Co_3O_4/N-rmGO	N. A.	4-8	0.10	0.930 (RHE)	0.930	4.0	31
NG/CNT/Co_3O_4	N. A.	100	N. A.	-0.060 (Ag/AgCl)[d]	0.907	3.97	32
Co_3O_4@C-MWCNTs	235	10-25	0.29	0.890 (RHE)	0.890	3.90	33
Co_3O_4@N-C	N. A.	20	0.30	0.950 (RHE)	0.950	3.93	34
Co_3O_4/NPGC	145	10	0.21	0.970 (RHE)	0.970	~4.0	35
Co_3O_4/CNW-C	121	5	0.13	-0.150 (SCE)	0.862	3.98	36
CoO_x/hNCNCs	N. A.	1.2-5	0.01	-0.071 (Ag/AgCl)[b]	0.907	3.75	37
Co-S/G-3	296.9	~1000	0.32	0.930 (RHE)	0.930	~3.90	38
G-Co/CoO	N. A.	~10	0.02 mg	-0.099 (Ag/AgCl)[d]	0.867[e]	3.90	39
CoO@NS-CSs	667	N. A.	0.41	0.946 (RHE)	0.946	~4.0	40
CoO/hi-Mn_3O_4	N. A.	150	0.26	N. A.	N. A.	3.8	41
$ZnMnCoO_4$	30.9	>500	0.25	1.0 (RHE)	1.0	3.80-3.93	42
$CoFe_2O_4$/hNCNC	N. A.	18.1	0.12	0.966 (RHE)	0.966	3.82-3.95	9
$MnCo_2O_4$-900	~50	~400	0.0102	~0.9 (RHE)	~0.9	~3.9	43
{Co}[FeCo]O_4/NG	N. A.	16	0.6	0.980 (RHE)	0.980	3.90	44
$ZnCo_2O_4$/N-CNT	159	3.0-3.5	0.2	0.950 (RHE)	0.950	3.80	45
P-CNCo-20	1225	~50	0.1	-0.08 (Ag/AgCl)[c]	0.893	3.90	46
Co SAs/N-C(900)	1393	Single atom	0.408	0.982 (RHE)	0.982	3.96	47
Co-ISAS/p-CN	380	Single atom	N. A.	N. A.	$E_{1/2}$=0.838	3.90	48
ZnN_x/BP	1383	Single atom	0.39	0 (SCE)	1.012	~4.0	49

Note: [a] N.A.: not available. [b] 3.0 mol L^{-1} KCl. [c] 3.5 mol L^{-1} KCl. [d] sat. KCl. [e] The values were estimated from the figures of the references. [f] All of the measured potentials were converted to reversible hydrogen electrode (RHE) by adding a value of 0.978 V for Ag/AgCl (3.0 mol L^{-1} KCl), 0.973 V for Ag/AgCl (3.5 mol L^{-1} KCl), 0.966 V for Ag/AgCl (sat. KCl), 0.866 V for Hg/HgO (1.0 mol L^{-1} KOH), and 1.012 V for saturated calomel electrode (SCE).
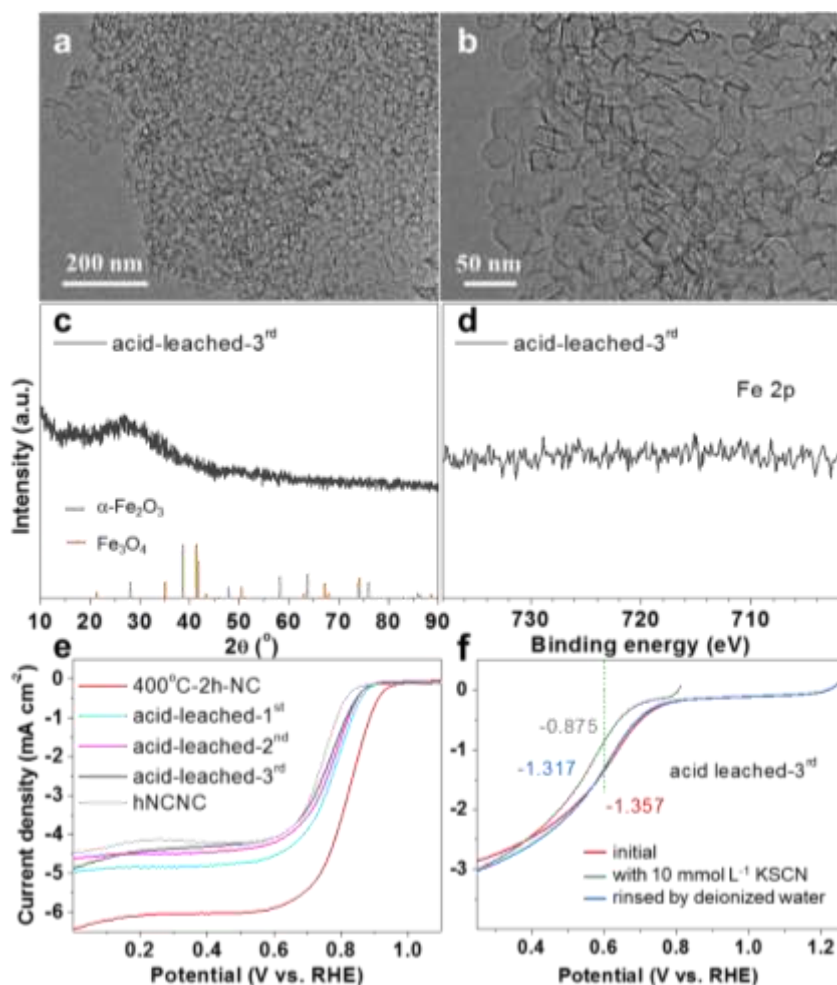
Fig. S12. (a-d) TEM (a,b), XRD (c) and XPS (Fe 2p) (d) characterizations of the 400°C-2h-NC catalyst after acid-leaching for three times. (e) LSV curves of the 400°C-2h-NC catalyst as-prepared and after acid-leaching for one, two, and three times. The curve of pure hNCNC was presented for comparison. (f) LSV curves of the acid-leached-3rd catalyst in O_2-saturated 0.1 mol L^{-1} HClO$_4$ with or without 10 mmol L^{-1} KSCN in turn.

No iron oxide nanocrystals, diffraction peaks and Fe signal were observed for the catalyst after acid-leaching for three times (Fig. S12a-d). It is reported that thiocyanate ion (SCN$^-$) can poison ferric iron active sites in catalyzing ORR below 0.70 V in acidic medium,[50-53] which could be used as an indicator to examine the residual metal ions after acid leaching. The SCN$^-$ poisoning experiment of the acid-leached-3rd catalyst was firstly carried out in O_2-saturated 0.1 mol L^{-1} HClO$_4$ without or with 0.01 mol L^{-1} KSCN. It can be seen that the reduction potential and current density @0.60 V decrease by about 0.1 V and 0.482 mA cm^{-2} after the addition of 0.01 mol L^{-1} KSCN (Fig. S10f). This result suggests that the residual ferric iron active sites can be blocked by SCN$^-$ in catalyzing ORR in acid medium. We then simply rinsed the blocked electrode by deionized water and measured it in O_2-saturated HClO$_4$ without 0.01 mol L^{-1} KSCN again, the ORR activity almost recovered to the initial values since SCN$^-$ easily dissociates from ferric iron sites due to the low stability constant of complexes (Fig. S12f).[54] So, the SCN$^-$ poisoning experiment confirms the existence of residual trace iron species and thereof leading the slightly better ORR activity than that of hNCNC support (Fig. S12e).

Details in theoretical calculations

All the calculations in this study were performed with the program package DMol^3 in Materials Studio (version 3.0) of Accelrys Inc. at the density functional theory level. In the DMol^3 method,[55-57] the physical wavefunctions are expanded in terms of accurate numerical basis sets. We used the double-numeric quality basis set with polarization functions (DNP). The core treatment of density functional semicore pseudopotential (DSPP) with a simple potential, and includes some degree of relativistic correction was used. Pseudopotentials Perdew Burke Ernzerhof (PBE) version of the generalized gradient approximation (GGA) was used to describe exchange-correlation functional.[58-60] A 1×1×1 *k*-point sampling was also used.

The heterostructural models are usually stressed due to the lattice mismatch between the two components. By checking all possible combinations, α-Fe$_2$O$_3$ (104) and Fe$_3$O$_4$ (220) were selected to build the heterostructure due to the minimum lattice mismatch (~11.7%). For the isolate models, the Fe atoms located on the surface were selected as the ORR active center, while for the heterostructural model, the Fe atom the surface of the heterojunction was chosen as the active center (See the blue arrow indicator of Fig. S13). All the vacuum thicknesses were set to 20 Å to minimize the interactions between adjacent images. All edged iron atoms were saturated by oxygen to eliminate dangling bonds. Accordingly, the ORR process including the successive steps of O$_2$ hydrogenation to OOH*, O-O bond scission of OOH* to O*, protonation of O* to OH*, and OH* removal to form OH$^-$ for the different models are calculated.

The calculation of ORR free energy diagram was performed according to the method proposed by Nørskov et al.[61] And the free energy was calculated by the equation G = E + ZPE − TS, where E is the total energy, ZPE is the zero-point energy, T is the temperature in kelvin, and S is the entropy. The vibrational frequencies were calculated in the harmonic normal-mode approximation to determine ZPE and the entropy contributions. The free energy of (H$^+$ + e$^-$) under standard conditions at pH 0 and U = 0 is taken to be 1/2H$_2$. The free energy of O$_2$ was obtained from the reaction O$_2$ + 2H$_2$ → 2H$_2$O, with a known free energy decrease of 4.92 eV. The free energy of H$_2$O(l) was derived from the equation $G_{H2O(l)} = G_{H2O(g)} + RT \times \ln(p/p_0)$, where R is the ideal gas constant, T = 298.15 K, p = 0.035 bar, and p_0 = 1 bar. The free energy of OH$^-$ was derived from the equation $G_{OH^-} = G_{H2O(l)} - G_{H^+}$, where $G_{H^+} = 1/2G_{H2} - pH \times k_BT \ln10$, k_B is the Boltzmann constant. The solution effect was considered by adding four water molecules around the absorbates.

The ORR process in alkaline medium

The complete 4e ORR process in alkaline medium is described by equations S5~S8 and illustrated by Fig. S11. The asterisk (*) indicates the adsorption sites or the species in chemisorbed state. The calculated free energy changes (ΔG) for each ORR step are denoted as ΔG_1~ΔG_4, respectively.

$$O_2 + 2H_2O + 4e^- + {}^* \rightarrow OOH^* + OH^- + H_2O + 3e^- \tag{S5}$$

$$OOH^* + OH^- + H_2O + 3e^- \rightarrow O^* + 2OH^- + H_2O + 2e^- \tag{S6}$$

$$O^* + 2OH^- + H_2O + 2e^- \rightarrow OH^* + 3OH^- + e^- \tag{S7}$$

$$OH^* + 3OH^- + e^- \rightarrow 4OH^- + {}^* \tag{S8}$$
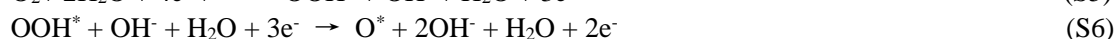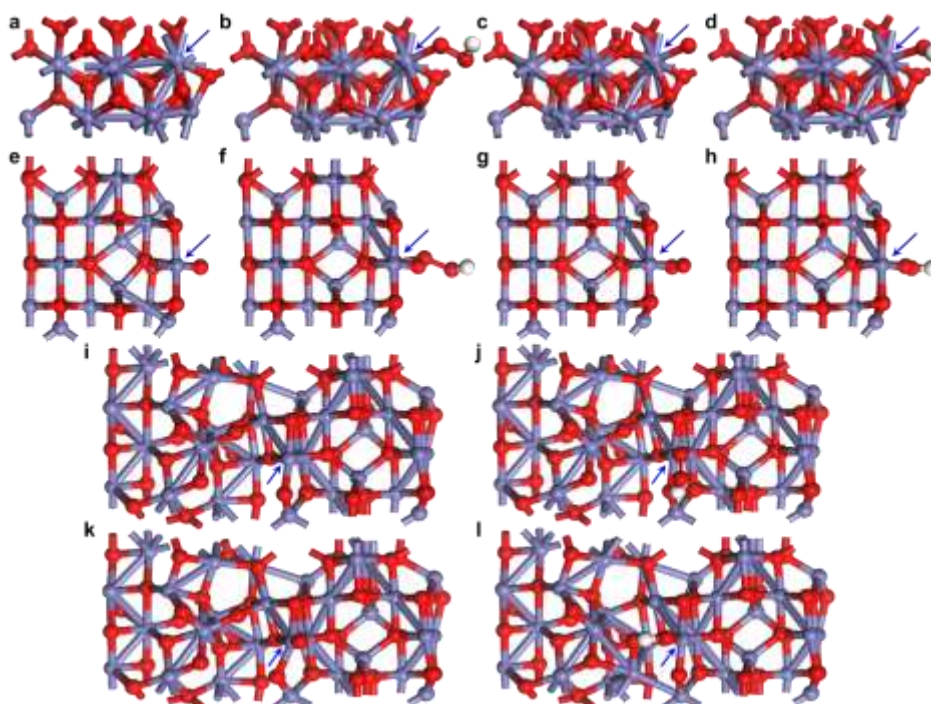
Fig. S13. The ORR process on α-Fe₂O₃ (a-d), Fe₃O₄ (e-h) and hetero-α-Fe₂O₃/Fe₃O₄ (i-l) in alkaline medium. Fe_grey, O_red. H_white. The arrowed Fe atoms are chosen as active centers.

As known, the overpotential (η) in theoretical calculation plays a crucial role for describing the ORR activity of electrocatalysts, which can be calculated as the Gibbs free energy differences (ΔG) for each reaction step[62, 63]: η=Max[ΔG_1, ΔG_2, ΔG_3, ΔG_4]/e-0.46 [V].

Table S4 ΔG for each ORR step at U=0 V (Unit: eV)

Models	ΔG_1	ΔG_2	ΔG_3	ΔG_4	η (V)
Hetero-α-Fe₂O₃/Fe₃O₄	-1.14	-0.75	-0.67	0.72	0.68
Fe₃O₄	-1.52	-1.23	-2.27	3.18	2.72
α-Fe₂O₃	-4.73	1.45	0.11	1.33	4.27

References

(1) Hu, C.; Xiao, Y.; Zhao, Y.; Chen, N.; Zhang, Z.; Cao, M.; Qu, L. *Nanoscale* **2013**, *5*, 2726.
(2) Lyu, Z.; Xu, D.; Yang, L.; Che, R.; Feng, R.; Zhao, J.; Li, Y.; Wu, Q.; Wang, X.; Hu, Z. *Nano Energy* **2015**, *12*, 657.
(3) Grosvenor, A. P.; Kobe, B. A.; Biesinger, M. C.; McIntyre, N. S. *Surf. Interface Anal.* **2004,** *36*, 1564.
(4) Lu, J. Z.; Yang, L. J.; Xu, B. L.; Wu, Q.; Zhang, D.; Yuan, S. J.; Zhai, Y.; Wang, X. Z.; Fan, Y. N.; Hu, Z. *ACS Catal.* **2014,** *4*, 613.
(5) Qiu, K.; Chai, G.; Jiang, C.; Ling, M.; Tang, J.; Guo, Z. *ACS Catal.* **2016**, *6*, 3558.
(6) Lu, X. F.; Gu, L. F.; Wang, J. W.; Wu, J. X.; Liao, P. Q.; Li, G. R. *Adv. Mater.* **2017,** *29*, 1604437.
(7) Tan, B. J.; Klabunde, K. J.; Sherwood, P. M. *J. Am. Chem. Soc.* **1991,** *113*, 855.
(8) Li, C.; Han, X.; Cheng, F.; Hu, Y.; Chen, C.; Chen, J. *Nat. Commun.* **2015,** *6*, 7345
(9) Fan, H.; Yang, L.; Wang, Y.; Zhang, X.; Wu, Q.; Che, R.; Liu, M.; Wu, Q.; Wang, X.; Hu, Z. *Sci. Bull.* **2017,** *62*, 1365.
(10) Zhang, H. T.; Chen, X. H. *Nanotechnology* **2006,** *17*, 1384.
(11) Feng, H.; Ma, J.; Hu, Z. *J. Mater. Chem.* **2010,** *20*, 1702.
(12) Arrigo, R.; Havecker, M.; Wrabetz, S.; Blume, R.; Lerch, M.; McGregor, J.; Parrott, E. P.;

Zeitler, J. A.; Gladden, L. F.; Knop-Gericke, A.; Schlogl, R.; Su, D. S. *J. Am. Chem. Soc.* **2010,** *132* (28), 9616.

(13) Zhao, J.; Lai, H.; Lyu, Z.; Jiang, Y.; Xie, K.; Wang, X.; Wu, Q.; Yang, L.; Jin, Z.; Ma, Y.; Liu, J.; Hu, Z. *Adv. Mater.* **2015,** *27* (23), 3541.

(14) Wang, D.; Su, D. *Energ. Environ. Sci.* **2014,** *7* (2), 576.

(15) Strelko, V. V.; Kuts, V. S.; Thrower, P. A. *Carbon* **2000,** *38* (10), 1499.

(16) Ren, S.; Ma, S.; Yang, Y.; Mao, Q.; Hao, C. *Electrochim. Acta* **2015,** *178*, 179-89.

(17) Dhavale, V. M.; Singh, S. K.; Nadeema, A.; Gaikwad, S. S.; Kurungot, S. *Nanoscale* **2015,** *7*, 20117.

(18) Sun, M.; Dong, Y.; Zhang, G.; Qu, J.; Li, J. *J. Mater. Chem. A* **2014,** *2*, 13635.

(19) Mohanraju, K.; Cindrella, L. *RSC Adv.* **2015,** *5*, 39455.

(20) Su, Y.; Jiang, H.; Zhu, Y.; Yang, X.; Shen, J.; Zou, W.; Chen, J.; Li, C. *J. Mater. Chem. A* **2014,** *2*, 7281.

(21) Wu, Z. S.; Yang, S.; Sun, Y.; Parvez, K.; Feng, X.; Müllen, K. *J. Am. Chem. Soc.* **2012,** *134*, 9082.

(22) Yang, H.; Wang, H.; Ji, S.; Linkov, V.; Wang, R. *Int. J. Hydrogen Energy* **2014,** *39*, 3739.

(23) He, T.; Li, Z.; Sun, Z.; Chen, S.; Shen, R.; Yi, L.; Deng, L.; Yang, M.; Liu, H.; Zhang, Y. *RSC Adv.* **2015,** *5*, 77296.

(24) Liu, S.; Dong, Y.; Zhao, C.; Zhao, Z.; Yu, C.; Wang, Z.; Qiu, J. *Nano Energy* **2015,** *12*, 578.

(25) Ma, Y.; Wang, H.; Key, J.; Linkov, V.; Ji, S.; Mao, X.; Wang, Q.; Wang, R. *Int. J. Hydrogen Energy* **2014,** *39*, 14777.

(26) Zhan, Y.; Xu, C.; Lu, M.; Liu, Z.; Lee, J. Y. *J. Mater. Chem. A* **2014,** *2*, 16217.

(27) Tan, Y. M.; Xu, C. F.; Chen, G. X.; Fang, X. L.; Zheng, N. F.; Xie, Q. J. *Adv. Funct. Mater.* **2012,** *22*, 4584.

(28) Duan, J.; Chen, S.; Dai, S.; Qiao, S. Z. *Adv. Funct. Mater.* **2014,** *24*, 2072.

(29) Duan, J.; Zheng, Y.; Chen, S.; Tang, Y.; Jaroniec, M.; Qiao, S. *Chem. Commun.* **2013,** *49* (70), 7705.

(30) Gao, S.; Geng, K. *Nano Energy* **2014,** *6*, 44.

(31) Kumar, K.; Canaff, C.; Rousseau, J.; Arrii-Clacens, S.; Napporn, T. W.; Habrioux, A.; Kokoh, K. B. *J. Phys. Chem. C* **2016,** *120*, 7949.

(32) Li, S. S.; Cong, H.-P.; Wang, P.; Yu, S. H. *Nanoscale* **2014,** *6*, 7534.

(33) Li, X.; Fang, Y.; Lin, X.; Tian, M.; An, X.; Fu, Y.; Li, R.; Jin, J.; Ma, J. *J. Mater. Chem. A* **2015,** *3*, 17392.

(34) Zhang, G.; Li, C.; Liu, J.; Zhou, L.; Liu, R.; Han, X.; Huang, H.; Hu, H.; Liu, Y.; Kang, Z. *J. Mater. Chem. A* **2014,** *2*, 8184.

(35) Li, G.; Wang, X.; Fu, J.; Li, J.; Park, M. G.; Zhang, Y.; Lui, G.; Chen, Z. *Angew. Chem., Int. Ed.* **2016,** *55*, 4977.

(36) Liu, S.; Li, L.; Ahn, H. S.; Manthiram, A. *J. Mater. Chem. A* **2015,** *3*, 11615.

(37) Chen, S.; Wang, L.; Wu, Q.; Li, X.; Zhao, Y.; Lai, H.; Yang, L.; Sun, T.; Li, Y.; Wang, X.; Hu, Z. *Sci. China Chem.* **2015,** *58*, 180.

(38) Odedairo, T.; Yan, X.; Ma, J.; Jiao, Y.; Yao, X.; Du, A.; Zhu, Z. *ACS Appl. Mater. Interface* **2015,** *7*, 21373.

(39) Guo, S.; Zhang, S.; Wu, L.; Sun, S. *Angew. Chem. Int. Ed.* **2012,** *51*, 11770.

(40) Chen, L.; Guo, X.; Zhang, G. *J. Power Sources* **2017,** *360*, 106.

(41) Guo, C.; Zheng, Y.; Ran, J.; Xie, F.; Jaroniec, M.; Qiao, S. Z. *Angew. Chem. Int. Ed.* **2017,** *56*, 8539.

(42) Wang, H.; Liu, R.; Li, Y.; Lü, X.; Wang, Q.; Zhao, S.; Yuan, K.; Cui, Z.; Li, X.; Xin, S.; Zhang, R.; Lei, M.; Lin, Z. *Joule* **2018,** *2* (2), 337-48.

(43) Wei, C.; Feng, Z.; Scherer, G. G.; Barber, J.; Shao-Horn, Y.; Xu, Z. J. *Adv. Mater.* **2017,** *29* (23), 1606800.

(44) Wu, G.; Wang, J.; Ding, W.; Nie, Y.; Li, L.; Qi, X.; Chen, S.; Wei, Z. *Angew. Chem. Int. Ed.* **2016,** *55* (4), 1340-4.

(45) Liu, Z. Q.; Cheng, H.; Li, N.; Ma, T. Y.; Su, Y. Z. *Adv. Mater.* **2016,** *28* (19), 3777-84.

(46) Chen, Y. Z.; Wang, C.; Wu, Z. Y.; Xiong, Y.; Xu, Q.; Yu, S. H.; Jiang, H. L. *Adv. Mater.* **2015,** *27* (34), 5010-6.

(47) Yin, P.; Yao, T.; Wu, Y.; Zheng, L.; Lin, Y.; Liu, W.; Ju, H.; Zhu, J.; Hong, X.; Deng, Z.; Zhou, G.; Wei, S.; Li, Y. *Angew. Chem. Int. Ed.* **2016,** *55* (36), 10800-5.

(48) Han, A.; Chen, W.; Zhang, S.; Zhang, M.; Han, Y.; Zhang, J.; Ji, S.; Zheng, L.; Wang, Y.; Gu, L.; Chen, C.; Peng, Q.; Wang, D.; Li, Y. *Adv. Mater.* **2018,** 1706508.

(49) Song, P.; Luo, M.; Liu, X. Z.; Xing, W.; Xu, W. L.; Jiang, Z.; Gu, L. *Adv. Funct. Mater.* **2017,** *27* (28), 1700802.

(50) Thorum, M. S.; Hankett, J. M.; Gewirth, A. A. *J. Phys. Chem. Lett.* **2011,** *2*, 295.

(51) Wang, Q.; Zhou, Z. Y.; Lai, Y. J.; You, Y.; Liu, J. G.; Wu, X. L.; Terefe, E.; Chen, C.; Song, L.; Rauf, M.; Tian, N.; Sun, S. G. *J. Am. Chem. Soc.* **2014,** *136*, 10882.

(52) Jiang, W. J.; Gu, L.; Li, L.; Zhang, Y.; Zhang, X.; Zhang, L. J.; Wang, J. Q.; Hu, J. S.; Wei, Z.; Wan, L. J. *J. Am. Chem. Soc.* **2016,** *138*, 3570.

(53) Sun, T.; Wu, Q.; Zhuo, O.; Jiang, Y.; Bu, Y.; Yang, L.; Wang, X.; Hu, Z. *Nanoscale* **2016,** *8*, 8480.

(54) Speight, J. G. *Lange's Handbook of Chemistry*; McGraw-Hill New York, **2005**.

(55) Delley, B. *J. Chem. Phys.* **1990,** *92* (1), 508-17.

(56) Delley, B. *J. Phys. Chem.* **1996,** *100* (15), 6107-10.

(57) Orita, H.; Itoh, N.; Inada, Y. *Chem. Phys. Lett.* **2004,** *384* (4), 271-6.

(58) Hohenberg, P.; Kohn, W. *Phys. Rev.* **1964,** *136* (3B), B864-71.

(59) Kohn, W.; Sham, L. J. *Phys. Rev.* **1965,** *140* (4A), A1133-8.

(60) Payne, M. C.; Teter, M. P.; Allan, D. C.; Arias, T. A.; Joannopoulos, J. D. *Rev. Modern Phys.* **1992,** *64* (4), 1045-97.

(61) Nørskov, J. K.; Rossmeisl, J.; Logadottir, A.; Lindqvist, L.; Kitchin, J. R.; Bligaard, T.; Jónsson, H. *J. Phys. Chem. B* **2004,** *108* (46), 17886-92.

(62) Feng, J. X.; Ye, S. H.; Xu, H.; Tong, Y. X.; Li, G. R. *Adv. Mater.* **2016**, *28* (23), 4698-703.

(63) Bai, X.; Wang, Q.; Xu, G.; Ning, Y.; Huang, K.; He, F.; Wu, Z. J.; Zhang, J. *Chem.-Eur. J.* **2017**, *23* (66), 16862-70.